A high-speed-modulated retro-reflector for lasers using an acousto-optic modulator

G. Spirou, I. Yavin, M. Weel, A. Vorozcovs, A. Kumarakrishnan, P.R. Battle, and R.C. Swanson

Abstract: We have used an acousto-optic modulator (AOM) to impose a frequency-modulated signal on an incident laser beam. The incident laser beam is focussed into the AOM where it undergoes Bragg diffraction and is then retro-reflected. The diffracted beam is also retro-reflected so that it is diffracted again by the AOM and overlaps the incident beam. The overlapped beams are frequency shifted with respect to each other. These features allow us to detect the frequency-modulated signal with high signal-to-noise ratio using heterodyne detection. Since the optical setup is simple and can be made very compact, this device may be ideal for certain forms of high-speed, free-space optical communication. We demonstrate a 1 MHz data transmission rate in the Bragg regime. We measured the acceptance angle of the device and find that it is limited only by the divergence of the focussed laser beam and the divergence of the acoustic waves in the AOM crystal. We have also studied the range of acoustic frequencies and drive power of the AOM, for which the retro-reflected beam can be detected with adequate signal to noise.

PACS No.: 42.60.–V, 42.62.Cf, 42.62.Fi, 42.79.Sz, 42.79.Hp

Résumé : Nous avons utilisé un modulateur acousto-optique (AOM) pour imposer un signal modulé en fréquence à un rayon laser incident. Le faisceau laser est focalisé sur l'AOM où il subit une diffraction de Bragg et est rétro-réfléchi. Le faisceau diffracté est également rétro-réfléchi, de telle façon qu'il est diffracté de nouveau par l'AOM et se superpose au faisceau incident. Les faisceaux superposés sont déplacés en fréquence l'un par rapport à l'autre. Ces propriétés nous permettent de détecter le signal modulé en fréquence avec un fort rapport signal sur bruit en utilisant un détecteur hétérodyne. Parce que le montage optique est simple et qu'il peut être très compact, il peut être idéal pour certaines formes de communications optiques à haute vitesse dans un espace libre. Nous avons atteint un taux de transmission de données à 1 MHz en régime de Bragg. Nous avons mesuré l'angle de réception du dispositif et trouvons qu'il est limité seulement par la divergence du faisceau laser modulé et la divergence des ondes acoustiques du cristal AOM. Nous avons aussi étudié

Received 9 July 2002. Accepted 3 December 2002. Published on the NRC Research Press Web site at http://cjp.nrc.ca/ on 5 June 2003.

G. Spirou, I. Yavin,[1] M. Weel, A. Vorozcovs, and A. Kumarakrishnan.[2] Department of Physics, York University, 4700 Keele St., Toronto, ON M3J 1P3, Canada.
P.R. Battle. AdvR Inc., 910 Technology Blvd., Suite K, Bozeman, MT 59718, U.S.A.
R.C. Swanson. Resonon Inc., 611 N. Wallace 7, Bozeman, MT 59715, U.S.A.

[1]Present address: Department of Physics, Harvard University, Cambridge, MA 02138, U.S.A.
[2]Corresponding author (e-mail: akumar@yorku.ca).

 doi: 10.1139/P03-047

le domaine des fréquences acoustiques et la puissance de modulation du AOM, pour lequel le faisceau rétro-réfléchi peut être détecté avec un niveau de signal sur bruit adéquat.

[Traduit par la Rédaction]

1. Introduction

During the last decade there has been an exponential increase in communication rates using optical fibers. Although typical communication rates associated with internet connections are ~10–100 MHz, transmission rates of the order of 40 GHz have been achieved. Since free-space communication avoids the use of fiber installation, it may offer cost-efficient solutions in certain cases [1]. Examples where this may be effective include communication between high-rise towers, temporary communication terminals, relay stations on hazardous industrial floors, and communication with moving platforms, such as satellites. Typically, these applications involve two laser sources to establish a link. Alternatively, a remote retro-reflector can be used to encode information on an incident laser beam.

A demonstration of an amplitude-modulated retro-reflector for a ground-based laser beam is described in ref. 2. In this experiment, the retro-reflector was carried on a high-altitude balloon. The retro-reflector consisted of a liquid crystal panel mounted in front of a "cat's eye" corner cube reflector. Although the acceptance angle of this device was ~15°, the modulation rate of a ground-based cw (continuous wave) laser was limited to ~10 kHz. Reference 3 describes a compact retro-reflector that can communicate at a much higher rate (~10 MHz). This device is based on a multiple quantum well modulator. Although it has a field of view of ~20°, the on–off contrast ratio depends on the fabrication process and varies between 2:1 and 4:1. We have recently demonstrated a retro-reflector based on electro-optic phase modulation that is capable of achieving a field of view of ~15° and a data transmission rate of a few GHz [4]. The retro-reflector discussed in this paper uses an AOM (acousto-optic modulator) operating in the Bragg regime [5–7] and can achieve communication rates similar to those given in ref. 3. It has the potential to achieve data transmission rates of ~1 GHz if operated in the Raman–Nath regime. This device has the desirable characteristics discussed in refs. 2 and 3 such as low cost and low-power consumption. An important advantage is that the retro-reflected signal is detected using heterodyne detection as described in ref. 4. Therefore, the signal can be measured with a high signal-to-noise ratio against a zero background. The advantages of using heterodyne techniques for free-space communication have been addressed in ref. 8. However, the field of view of the device in the Bragg regime is limited to about ~1°. As a result, we expect this device to be better suited for a short range (~1 km) communication link. In this article, we use an AOM operating in the Bragg regime [9] to achieve a high-speed frequency-modulated retro-reflector. The AOM operates in a dual-pass configuration. Similar configurations are used extensively in laser spectroscopy [10]. The Bragg condition given by

$$2\lambda_s \sin\theta_B = \lambda_L \tag{1}$$

is satisfied in our experiments. Here, λ_s is the acoustic wavelength in the AOM crystal, θ_B is the Bragg angle and λ_L is the wavelength of the laser. Bragg scattering corresponds to a regime in which the incident beam undergoes mirror-like reflection from the acoustic wave front. In this regime, the diffracted beam and the incident beam remain in phase over the entire acoustic wave front [11]. Figure 1 illustrates the basic features of this device. When a sequence of radio frequency (RF) pulses is applied to the AOM, the incoming laser beam is diffracted and retro-reflected through the AOM. If the propagation time τ_p through the optical setup involving the AOM is shorter or comparable to the RF pulse width τ_w, the retro-reflected diffracted beam will interact with the same RF pulse. The device can be aligned so the twice-diffracted beam overlaps with the undiffracted retro-reflected beam. This feature allows the retro-reflected signal to be detected by the presence or absence of frequency modulation.

The data transmission rate for high-speed frequency modulation is determined by the spacing T between pulses in a temporal sequence. This requires that the rise time of the diffracted optical pulses

Fig. 1. AOM-based retro-reflector: The laser station, S sends a cw laser beam to the AOM module and the frequency-shifted beam is retro-reflected.

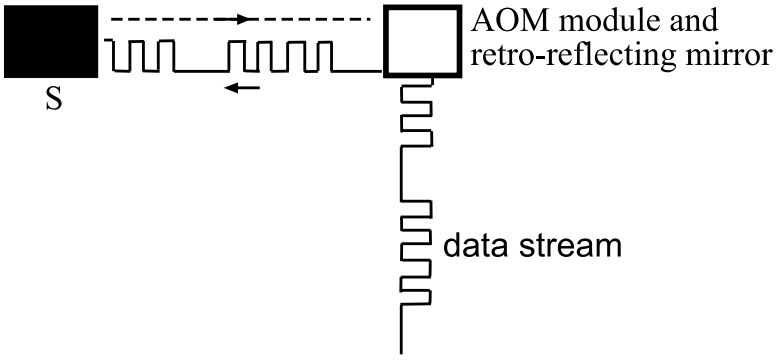

from the AOM τ_r and the RF pulse width τ_w should be comparable or smaller than T, i.e., $\tau_r, \tau_w \leq T$. Since the rise time depends on the propagation time of the acoustic wave across the laser beam, it is necessary to focus the laser beam to the appropriate waist size, ω_0. When an acoustic plane wave travels across a Gaussian laser beam the intensity of the diffracted beam as a function of time can be expressed as $I(t) \propto (1 - e^{-2t^2/\tau^2})$. The relationship between the rise time τ of the diffracted laser beam (10%–90%) and the $1/e^2$ diameter $2\omega_0$ of a Gaussian laser beam at the location of the AOM is given by

$$\tau_r = 0.84 \frac{2\omega_0}{V_s} \tag{2}$$

where V_s is the speed of sound in the AOM crystal. If the incident laser beam and the acoustic wave are plane waves, the retro-reflected signal will be observed only at the angular position of the AOM that satisfies the Bragg condition in (1).

When a Gaussian laser beam is focussed into the AOM, there is a range of k-vectors that can interact with the acoustic wave and satisfy the Bragg condition. In addition, since the acoustic wave has an angular divergence, the range of angular positions of the AOM for which the signal can be observed is further increased. It is therefore interesting to note that in the Bragg regime, the optical setup is relatively insensitive to misalignment. Since the AOM consists of a tuned RLC circuit, it is also possible to correct for effects of misalignment by varying the radio frequency and the drive power. The remainder of this paper is organized as follows: in Sect. 2, we discuss details of the experimental setup and the detection technique. In Sect. 3, we demonstrate a data transmission rate of 1 MHz, discuss the diffraction efficiency of the AOM and the measured signal-to-noise ratio for data transmission. In Sect. 4, we describe our studies of the field of view of this device. We compare our results to simple analytical models. These studies involve variations in the angular positions of the incident laser beam and the AOM. In Sect. 5, we study the effects of changing the applied radio frequency and RF power. In Sect. 6, we discuss the possibility of achieving a data transmission rate of $\sim$1 GHz.

2. Experimental setup

Figure 2 describes the optical setup. We use a fiber-coupled laser, which is operated at $\sim$15 mW and has a divergence angle of $\sim$1 mrad. The laser has a wavelength of $\lambda_L \sim 780$ nm, which is in the vicinity of the 800 nm band used for free-space communication. The incoming laser beam is sent through a polarizing-cube beam splitter, which reflects vertically polarized light and transmits horizontally polarized light. The retro-reflector consists of two identical convex lenses, an AOM, a quarter-wave plate and a mirror. The two lenses focus and re-collimate the beam before and after the AOM. The undiffracted and first-order-diffracted beams are sent through the quarter-wave plate and reflected from the mirror. This ensures that the beams are circularly polarized when they hit the mirror and have

Fig. 2. Experimental setup: P, polarizing cube beam splitter; D, detector; L, lens; f, focal length; M, mirror; Q, 1/4 wave plate; and f_s, frequency of the acoustic wave. Laser beams with frequencies ν_0 and $\nu_0 + 2f_s$ are collinear and overlap on the detector.

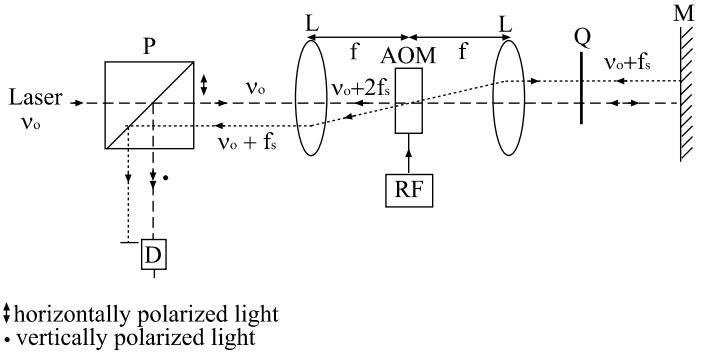

Fig. 3. Alternate experimental setup: P, polarizing cube beam splitter; D, detector; L, lens; f, focal length; M, mirror; Q, 1/4 wave plate; and BS, beam splitter. Laser beams with frequencies $\nu_0 + f_s$ and $\nu_0 + 2f_s$ are collinear and overlap on the detector.

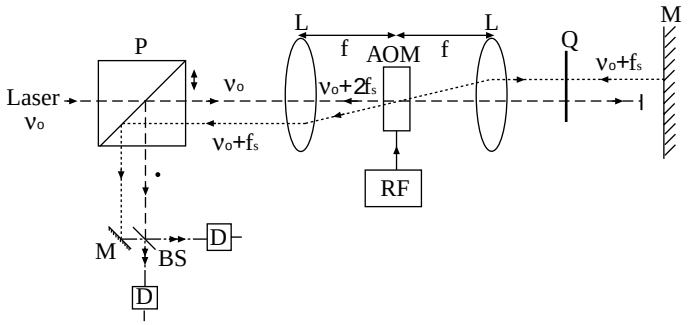

orthogonal linear polarization when they are retro-reflected through the quarter-wave plate. The beams are then re-focussed and re-collimated by the lenses on either side of the AOM. The twice-diffracted and undiffracted retro-reflected beams overlap with the direction of the incoming laser. These beams are reflected off the cube beam splitter and their beat signal is recorded on a SI-PIN photodiode. In this arrangement the beat frequency is the frequency difference between the undiffracted beam and the twice-diffracted beam (i.e., twice the operating frequency of the AOM). The resulting heterodyne signal can be recorded whenever the AOM is driven by the RF source. An alternative optical setup is shown in Fig. 3. It can be realized by using a balanced heterodyne detection system involving two detectors and an additional mirror and beam splitter after the cube beam splitter. In this arrangement the undiffracted beam is blocked after the first pass through the AOM. The beam splitter and mirror are then used to recombine the twice-diffracted and once-diffracted beams. The resulting beat frequency is half the beat frequency obtained using the setup in Fig. 2. Since the incident laser beam is blocked before retro-reflection, the detector records a signal only when the AOM is driven. Figures 4*a* and 4*b* provide pictorial representations of the beat signal for the optical setups shown in Figs. 2 and 3, respectively. Although the figures display different DC offsets, we note that there is no inherent advantage of using either setup. This is because the heterodyne signals (shown in Fig. 4) can be mixed down to DC.

Fig. 4. Schematic representation of beat signal: (*a*) corresponds to Fig. 2 and (*b*) corresponds to Fig. 3. The two signals differ in the beat frequency and DC offset.

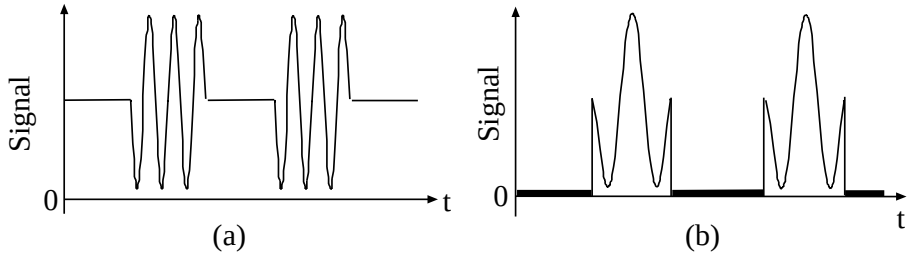

Fig. 5. Heterodyne signal recorded on photodiode: (A) pulse width ∼60 ns; pulse spacing = 1 μs and (B) expanded trace of a single pulse in Fig. 5A showing 120 MHz beat signal.

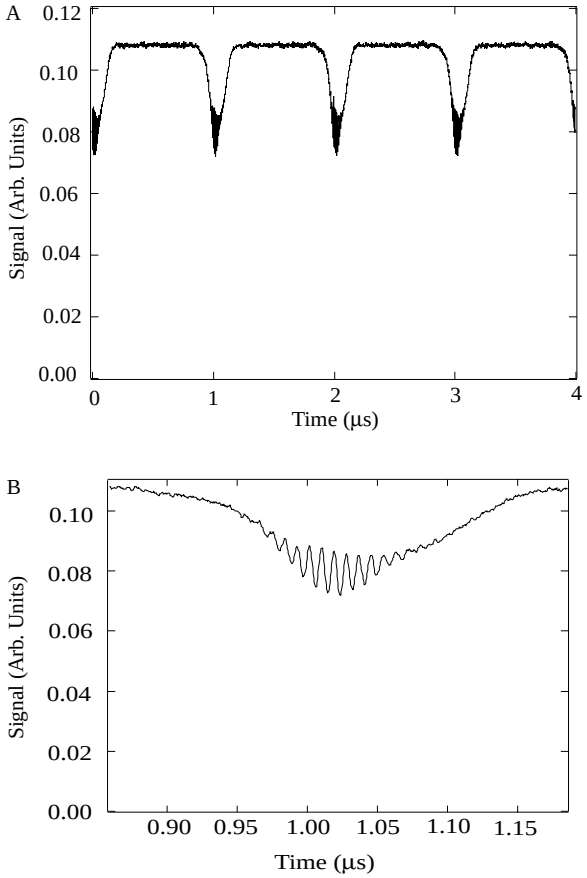

3. Data transmission

We have used the optical setup in Fig. 2 to demonstrate a 1 MHz communication rate. Identical lenses with focal length $f = 300$ mm and an AOM operating at 60 MHz were used. The repetition rate of the pulse generator driving the AOM limited the data transmission rate. A sequence of RF pulses ($\tau_w = 60$ ns) and a repetition rate of 1 MHz was used to drive the AOM. Figure 5A shows the corresponding heterodyne signal recorded by the photodiode (rise time = 1 ns).

Figure 5B is an expanded trace of a pulse in Fig. 5A. It is easy to see that the frequency-modulated

signal occurs at the beat frequency of 120 MHz. The decrease in the envelope amplitude is due to the loss of power from the undiffracted beam when the AOM is pulsed on. These data were obtained using a $1/e^2$ beam diameter of ~0.30 mm at the location of the AOM. The diameter was measured using the rise time of the diffracted laser pulse and the speed of sound in the crystal (TeO_2). We determined the speed of sound in the AOM crystal by measuring the Bragg angle as a function of radio frequency f_s and using (1). The measured value ($4.0 \times 10^3 \pm 10\%$ m/s) was in agreement with the published value (4200 m/s) [12]. We attribute the difference between the experimental and published values to the error in the measurement of the Bragg angle. For a single pass, the diffraction efficiency, η, is defined as the ratio of the first-order diffracted intensity I_1 to the incident laser intensity I_{INC}. Assuming an interaction between a plane acoustic wave and a plane optical wave, the expression for η is given by [13, 14]

$$\eta = \frac{I_1}{I_{INC}} = \sin^2\left(\frac{\pi L}{\lambda_L \cos\theta_B}\sqrt{\frac{M_2 I_s}{2}}\right) \tag{3}$$

where L is the interaction length of the laser beam with the acoustic wave, I_s is the intensity of the acoustic wave, θ_B is the Bragg angle, and M_2 is the figure of merit of the crystal. The acoustic intensity $I_s = P_a/HL$ where P_a is the average power and H is the height of the acoustic wave. Both H and L can be estimated from the size of the transducer. For the 60 MHz AOM used in our experiments, (3) predicts an efficiency of ~73%. The maximum diffraction efficiency was measured to be ~60%. The difference can be attributed to divergence angle associated with the laser beam and the acoustic wave. Using ~15 mW of incident laser power, the maximum dual-pass efficiency was ~35% in our experiments. The minimum dual-pass diffraction efficiency for which the heterodyne signal could be measured above the noise was found to be 0.03%. The signal can, therefore, be detected with an adequate signal-to-noise ratio over two orders of magnitude in intensity. This allows the optical setup to be operated over a wide range of radio frequencies and angular positions of the incident beam and the AOM.

4. Field of view

The divergence angle of the focussed laser beam and the divergence of the acoustic wave allows the Bragg condition to be satisfied for a range of angular positions of the AOM and for a range of incident angles of the laser beam. As a consequence, it is possible to test the dependence of the signal on angular displacements and determine the field of view. The field of view is the range of angular positions for which a signal can be observed. We have investigated the field of view by varying the angular position of the AOM as well as the angle of incidence. For these measurements, we compare the divergence angle of the laser beam obtained from spatial profile measurements to the data obtained by varying the angular position of the AOM and the angle of incidence. The divergence of the laser beam focussed into the AOM was inferred from measurements of the laser beam profile. The profile was measured using a knife edge scanning across the laser beam and measuring the transmitted laser intensity as a function of time [15]. The spatial profile was recorded at a number of positions after the lens located in front of the AOM (see Fig. 2). We modelled the spatial profile of the laser beam as a Gaussian given by

$$I_{INC} = I_L \exp\left(\frac{-r^2}{\omega(z)^2}\right) \tag{4}$$

here I_{INC} is the incident intensity, I_L is the maximum intensity of the beam, r is the transverse coordinate (see Fig. 6), and $\omega(z)$ is the $1/e^2$ beam waist as a function of position along the direction of propagation. $\omega(z)$ is given by

$$\omega(z) = \omega_0\left(1 + \left(\frac{z}{z_0}\right)^2\right)^{1/2} \tag{5}$$

Fig. 6. Gaussian laser beam profile showing the beam waist as a function of distance from focal plane. ω_0, waist at the focal plane; z_0, Rayleigh range; $\Delta\Theta_s$, divergence angle of the focussed laser beam; and θ, angle of any k-vector within divergence angle.

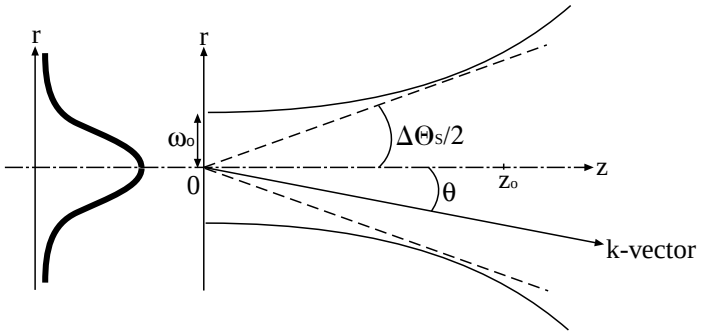

Here, the Rayleigh range z_0 is given by $z_0 = \pi\omega_0^2/\lambda_L$ and ω_0 is the $1/e^2$ waist at the focus of the lens ($z = 0$). From Fig. 6, we see that the divergence angle of the focussed laser beam $\Delta\Theta_s$ is approximated by

$$\frac{\Delta\Theta_s}{2} = \frac{\omega(z)}{z} \tag{6}$$

If $z/z_0 >> 1$, (5) can be simplified to $\omega(z) = \omega_0 z/z_0$. Using the expression for the Rayleigh range z_0, the divergence angle is given by

$$\Delta\Theta_s = \frac{2\lambda_L}{\pi\omega_0} \tag{7}$$

In our experiments, we fit the beam waist using (5) and obtained ω_0. The divergence angle $\Delta\Theta_s$ was then calculated using (7). Since the Gaussian beam contains a range of k-vectors, any given k-vector can be represented by an angle θ given by

$$\theta = \frac{r}{z} \tag{8}$$

we can use (6) and (8) to get

$$\frac{r^2}{\omega(z)^2} = \frac{4\theta^2}{\Delta\Theta_s^2} \tag{9}$$

It is, therefore, possible to express the intensity of the laser beam as a function of the angle θ

$$I_{INC} = I_L \exp\left(\frac{-\theta^2}{(\frac{\Delta\Theta_s}{2})^2}\right) \tag{10}$$

Equation (10) was used to model experimental results. For this experiment, the AOM was placed on a rotating stage placed after the focussing lens at the position of the minimum waist (ω_0). The intensity of the pulsed diffracted beam was then measured as a function of angular position.

Figure 7A shows the variation of the beam waist as a function of position using a 250 mm lens. The beam divergence obtained from the fit gives $\Delta\Theta_s = 3.6 \pm 0.5$ mrad. Figure 7B shows the intensity of the diffracted beam as a function of the angular position of the AOM. The AOM was driven at 110 MHz. We refer to the angular divergence obtained from a least-squares Gaussian fit with a functional form given

Fig. 7. (A) $1/e^2$ beam waist $\omega(z)$ versus z. The data are fit to (5); the fit gives $\Delta\Theta_s = 3.6 \pm 0.5$ mrad. (B) Intensity of first-order diffracted beam as a function of angular position of AOM placed at location of minimum waist in (A). Points represent experimental data and the continuous line represents a Gaussian fit based on (10). From $1/e^2$ points on the fit, $\Delta\Theta_{AOM} = 12.1 \pm 0.1$ mrad.

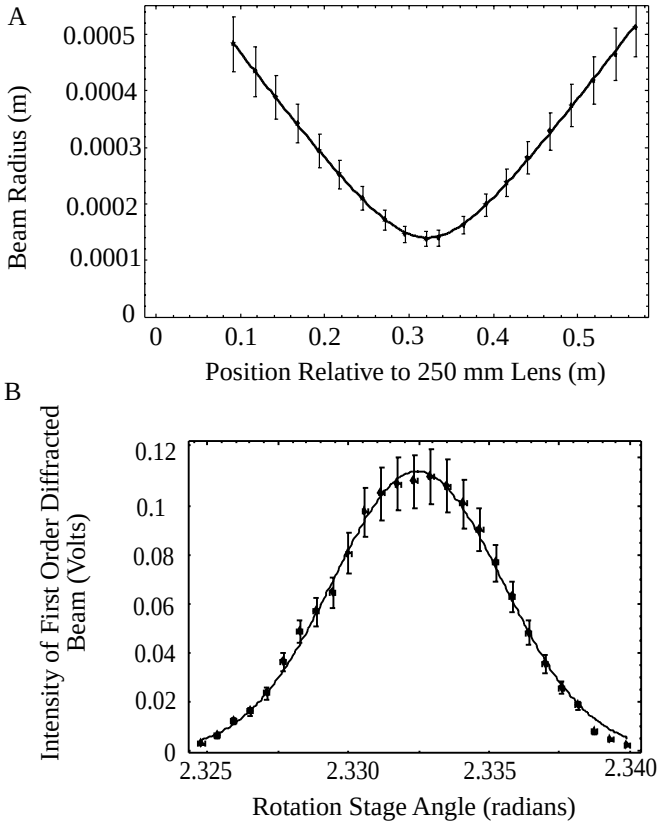

by (10) as $\Delta\Theta_{AOM}$. The continuous line in Fig. 7B represents the fit. The fit gives a $1/e^2$ divergence $\Delta\Theta_{AOM} = 12.1 \pm 0.1$ mrad. We attribute the discrepancy between the results for $\Delta\Theta_s$ and $\Delta\Theta_{AOM}$ due to the acoustic wave divergence $\Delta\Theta_A$, which is not considered in our analysis. Since we are not in a position to measure the divergence of the acoustic wave, we assume that it has a Gaussian profile with divergence angle $\Delta\Theta_A$. Our data for the angular range $\Delta\Theta_{AOM}$ can be modelled by adding $\Delta\Theta_A$ and $\Delta\Theta_s$ in quadrature. We therefore write

$$\Delta\Theta_{AOM} = \alpha_o \left(\Delta\Theta_A^2 + \Delta\Theta_s^2\right)^{1/2} \tag{11}$$

where α_o is a constant that represents the asymptotic value of (11). If $\Delta\Theta_A << \Delta\Theta_s$, $\Delta\Theta_s \approx \Delta\Theta_{AOM}$ and $\alpha_o \to 1$. We have measured the value of $\Delta\Theta_{AOM}$ as a function of $\Delta\Theta_s$ using five different lenses and the 110 MHz AOM. The focal lengths of the lenses used were 100, 125, 200, 250, and 400 mm. The results are summarized in Fig. 8.

The data are in agreement with the fit given by (11). From the fit, we obtain $\alpha_o = 1.3$ and $\Delta\Theta_A = 8.6$ mrad. The statistical uncertainties in these quantities are estimated to be $\pm 20\%$ and $\pm 14\%$, respectively. We conclude that (11) is an accurate representation of the variation of $\Delta\Theta_{AOM}$, which is the effective field of view of the device. A crude estimate of $\Delta\Theta_A$ using the physical dimensions of the transducer attached to the AOM crystal gives $\Delta\Theta_A \sim 15$ mrad, which is comparable to the value obtained from the fit (since the transducer consists of an array, the estimate has to be refined). We have

Fig. 8. Field of view measured by rotating AOM driven at 110 MHz. Points show $\Delta\Theta_{AOM}$ versus $\Delta\Theta_s$; the fit (continuous line) is given by (11).

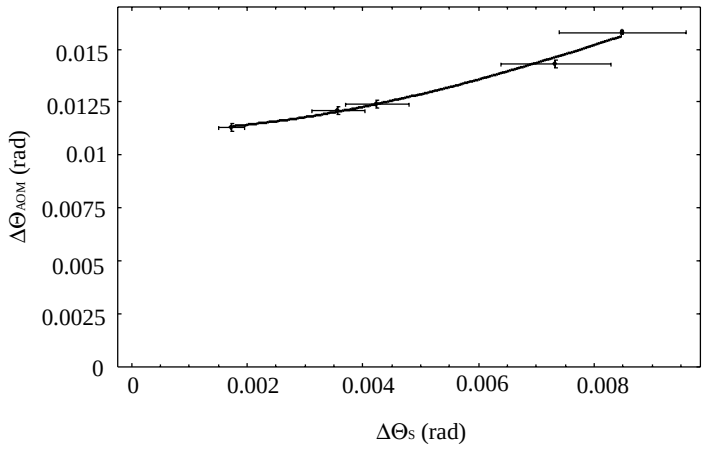

Fig. 9. Field of view measured by rotating AOM and by rotating the incident laser beam with AOM driven at 50 MHZ. Points (squares) show $\Delta\Theta_{AOM}$ versus $\Delta\Theta_s$; the fit (continuous line) is given by (11). Points (circles) show $\Delta\Theta_2$ versus $\Delta\Theta_s$; the fit (broken line) is given by (11).

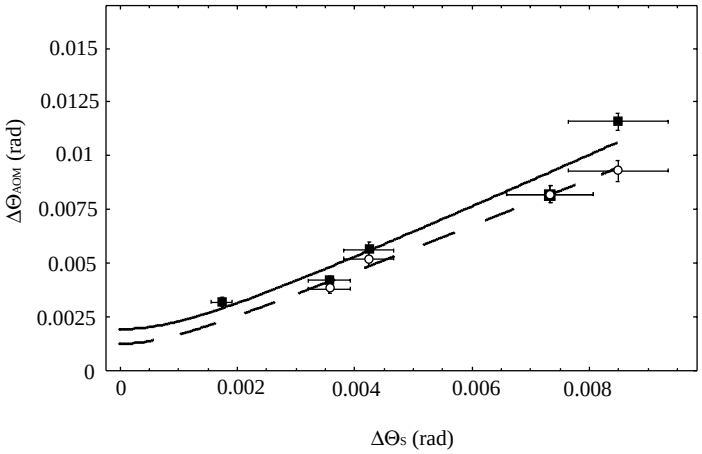

further tested the basis for this model by measuring the field of view of a 50 MHz AOM using the same set of lenses as in the previous experiment. The data (squares) are shown in Fig. 9. The corresponding hyperbolic fit (continuous line) gives $\alpha_o = 1.2 \pm 20\%$ and $\Delta\Theta_A = 1.5 \pm 60\%$ mrad. The value of α_o agrees with the expected value of unity within experimental error. Since the 50 MHz AOM has a larger transducer size than the 110 MHz AOM , the divergence of the acoustic wave $\Delta\Theta_A$ is expected to be much smaller (a crude estimate for $\Delta\Theta_A$ gives $\sim$5 mrad). Consequently, we expect the fit to be insensitive to the the value of $\Delta\Theta_A$. This is consistent with the statistical uncertainty obtained for $\Delta\Theta_A$ in this case.

We have so far obtained a measurement of the range of angular positions of the AOM (field of view) for which the retro-reflected signal can be measured. In refs. 2–4, the field of view refers to the range of incident angles for which the retro-reflector returns a signal. If the angle of incidence is varied in our experiments, the lens placed in front of the AOM changes the angle of incidence at the AOM and displaces the incident beam on the AOM crystal. However, a change in the angle of incidence is equivalent to an angular rotation of the AOM. In practice, the size of the lens and the active aperture of

Fig. 10. Thin-lens transformation of the angle of incidence. r is displacement of beam from principal axis due to change in angle of incidence θ_1. θ_2 is corresponding deviation from the angle of incidence at the AOM. d is distance between the laser (on rotation stage) and lens.

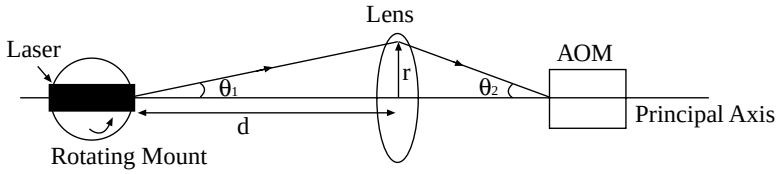

the AOM limit the range of incident angles for which a retro-reflected signal can be observed.

Figure 10 shows the change in the angle of incidence θ_2 at the AOM due to the lens for a change in the angle of incidence θ_1. The change is specified by the transformation matrix equations for a thin lens given by

$$r_2 = r_1 \tag{12}$$

$$\theta_2 = \frac{-r_1}{f} + \theta_1 \tag{13}$$

Here f is the focal length of the lens, r_1 and r_2 are the displacements of the beam from the principal axis before and after the lens, respectively. Since (12) and (13) are valid for a thin lens, $r_1 = r_2 = r$ as shown in Fig. 10. If the distance between the laser and the lens d is known, r can be expressed as $r = \tan\theta_1 d$. Accordingly, (13) can be expressed as

$$\theta_2 = \frac{-\tan\theta_1 d}{f} + \theta_1 \tag{14}$$

We have measured the range of angles θ_1 for which the intensity of the diffracted beam was observed. The angle of incidence was varied by rotating the laser mounted on a rotation stage and keeping the AOM at a fixed position. Using (14), the measured angles were transformed to corresponding values of θ_2. $\Delta\Theta_2$ was then obtained by fitting the data to the functional form of (10). This experiment was repeated using four of the five lenses used in the previous experiment. This is because the size of the active aperture of the AOM limited the range of incident angles at the AOM for the lens with $f = 400$ mm (we determined experimentally that the diffraction efficiency of the AOM was constant only over the active aperture of the AOM). The values of $\Delta\Theta_2$ were plotted as a function of $\Delta\Theta_s$ in Fig. 9 (circles). The broken line is a hyperbolic fit using the functional form of (11). The fit (broken line) gives $\alpha_o = 1.1 \pm 21\%$ and $\Delta\Theta_A = 1.1 \pm 167\%$ mrad. The values of α_o and $\Delta\Theta_A$ agree within experimental error to the fit parameters given by the continuous line shown in Fig. 9. This implies that the same acceptance angle has been measured by rotating the AOM and by changing the angle of incidence.

Our results show conclusively that the field of view of the device is dependent on the divergence angles of the optical and acoustic waves. The field of view can be $\sim 1^\circ$ in the Bragg regime. This is much larger than the beam-steering angular resolution required for short range ($\sim$1 km) free-space communication ($\sim$0.1 mrad).

5. Tuning range of AOM cavity

As mentioned in Sect. 1, the AOM consists of a tuned RLC circuit. Therefore, it is possible to operate the AOM at different radio frequencies and drive power and correct for effects of misalignment. We have measured the variation of the diffraction efficiency as a function of these parameters and used (3) to model our results. Equation (3) describes the efficiency of the first-order diffracted beam as a function of the acoustic wave intensity, I_s. As mentioned in Sect. 3, the equation is valid for optical and acoustic plane waves. I_s can be expressed in terms of the average RF power P_a and the area of the

acoustic wave defined by the height H and length L. Hence $I_s = P_a/HL$. The RF power is given by $P_a = \frac{1}{2} V_p I_p \cos\phi$. Here V_p is the applied peak voltage, I_p is the applied peak current driven through the RLC circuit with impedance Z, resistance R, inductance L_{IND}, and capacitance C. ϕ is the phase defined by $\cos\phi = R/Z$. Using Ohm's law, I_p can be expressed as $I_p = V_p/Z$. Using the expression for $\cos\phi$ the average acoustic intensity can be written as

$$I_s = \frac{V_p^2 R}{2HL(R^2 + (\omega L_{IND} - 1/\omega C)^2)} \tag{15}$$

where $Z = (R^2 + (\omega L_{IND} - 1/\omega C)^2)^{1/2}$ and omega is the angular frequency. It is given by $\omega = 2\pi f_s$ where f_s is the applied radio frequency. In these experiments, we have used an AOM operating in the Bragg regime with a cavity tuned to 60 MHz. A lens with $f = 300$ mm was used to focus the laser beam. The Rayleigh range ($\sim$9 cm) was larger than the length of the AOM crystal ($L \sim 5.5$ cm). The resistance of the RLC circuit is due to the transducer attached to the crystal. The circuit also consists of a discrete capacitor and inductor. The effective dimensions of the transducer are approximately H and L. We used these dimensions to infer the spatial extent of the acoustic wave. Since the laser beam used in our experiment has a Gaussian profile, the expression for I_{INC} in (3) must be modelled using (10). Since the intensity of the incident laser beam I_{INC} in (10) is a maximum (I_L) at the Bragg angle for 60 MHz (0.00551 rad), we can express the Gaussian intensity profile (10) in terms of the frequency of the acoustic wave f_s using (1). This expression is given by

$$I_{INC} = I_L \exp\left(\frac{-(0.00551 - \lambda_L f_s/2V_s)^2}{(\Delta\Theta/2)^2}\right) \tag{16}$$

Here, we have used the small-angle approximation $\sin\theta \sim \theta$ and V_s is the speed of sound in the AOM crystal. Equation (1) can be used to express $\cos\theta_B$ as a function of f_s

$$\cos\theta_B = \sqrt{1 - \frac{\lambda_L^2 f_s^2}{4V_s^2}} \tag{17}$$

The power of the RF oscillator used to drive the AOM varied as a function of frequency. The correction was experimentally determined and included in our analysis. Using (15)–(17) and the correction for the variation in RF power as a function of frequency in (3), the expression for the diffracted beam intensity I_1 as a function of frequency f_s can be expressed as

$$I_1 = I_L \exp\left(\frac{-(0.00551 - \lambda_L f_s/2V_s)^2}{(\Delta\Theta_{AOM}/2)^2}\right) \times \sin^2\left(\frac{\pi V_p}{2\lambda_L\sqrt{1 - \lambda_L^2 f_s^2/4V_s^2}}\sqrt{\frac{LM_2R}{H(R^2 + (\omega L_{IND} - 1/\omega C)^2)}}\right) \tag{18}$$

In the experiment, the AOM was positioned at the Bragg angle for 60 MHz. The first-order diffracted beam intensity was measured as a function of the angular position of the AOM and $\Delta\Theta_{AOM}$ was determined from a Gaussian fit using (10). The AOM was then realigned to maximize the intensity of the first-order diffracted beam. The diffracted beam intensity was then measured as a function of f_s. The data are shown in Fig. 11.

As f_s is varied, the diffracted intensity decreases smoothly on either side of 60 MHz. This effect is attributed to the divergence of the optical wave and the acoustic wave. When f_s is varied, various k-vectors in the incident beam satisfy the Bragg condition. When (18) is used to fit the data, the best fit (continuous line in Fig. 11) gives $L_{IND} = 7.9 \times 10^{-7} H$ and $C = 9.1 \times 10^{-12} F$. This is comparable to

Fig. 11. Intensity of first-order-diffracted beam as a function of radio frequency. Points represent experimental data and the continuous line represents the fit based on (18). 60 MHz corresponds to resonant frequency of AOM cavity.

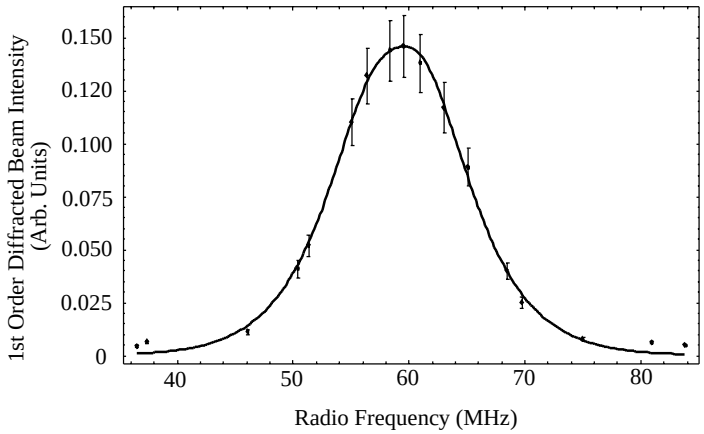

the value of L_{IND} estimated from the physical dimensions of the inductor ($5 \times 10^{-7} H$). However, it was not possible to estimate the value of the capacitance C. The values of L_{IND} and C obtained from the fit predict a resonant frequency of 59 MHz. This frequency is consistent with the known value (60 MHz) for the resonant frequency of the AOM cavity. Our results using the AOM in dual-pass configuration were the same within experimental error. The data indicate that the frequency tuning range of the device is $\sim \pm 10$ MHz. To correct for the effects of misalignment, the AOM can be operated off resonance. This will cause the signal-to-noise ratio to decrease. The decrease can be compensated by increasing the drive power. To demonstrate this idea, we have measured the RF power required to produce a constant first-order-diffracted intensity within the tuning range of the AOM cavity. The experiment was carried out by first aligning the AOM to maximize the intensity of the first-order-diffracted beam at the resonant frequency of 60 MHz. Then, the radio frequency was varied and the RF power required for observing a constant diffracted signal intensity was measured. Figure 12 shows the experimental results. When f_{s} is varied with respect to the central frequency of 60 MHz, the first-order-diffracted signal decreases due to the variation in the RF power associated with the source and the intensity profile of the laser beam. Thus, it is necessary to increase the RF power to obtain the same efficiency. To model the data, (18) was rearranged so that V_{p} could be expressed as a function of f_{s}. This equation was used to model the data with the same values for L_{IND} and C corresponding to the best fit from Fig. 11. The model is the continuous line in Fig. 12. Similar results were obtained with the dual-pass setup. The data show that it is possible to compensate for the loss of signal within a tuning range of $\sim \pm 10$ MHz with a modest increase in RF power.

6. High-speed communication

In the Bragg regime, it is possible to obtain a diffraction efficiency of ~50% using AOMs operating at ~200 MHz if the beam waist is comparable to the transducer size ($\omega_0 \sim 50\ \mu$m). Using $V_{\mathrm{s}} \sim 4.2 \times 10^2$ m/s and $\omega_0 \sim 50\ \mu$m, (2) gives $\tau_{\mathrm{r}} \sim 20$ ns. Using an optical pulse width comparable to the rise time, we estimate the maximum data transmission rate to be ~50 MHz. At this rate, the pulse width is sufficient to detect four or eight cycles of the beat frequency corresponding to the optical setups shown in Figs. 2 and 3, respectively. The experiments discussed in Sects. 3–5 were carried out in the Bragg regime ($L \gg \lambda_{\mathrm{s}}^2/\lambda_{\mathrm{L}}$). As discussed in Sect. 1, it is necessary to focus the beam tightly to achieve communication rates of ~1 GHz (AOMs with an operating frequency of up to 1.6 GHz are commercially available). However, this would require the AOM to operate in the Raman–Nath regime ($L \ll \lambda_{\mathrm{s}}^2/\lambda_{\mathrm{L}}$). Under these conditions, the intensity of the diffracted beam is insensitive to the angular

Fig. 12. Peak RF voltage as a function of frequency applied to AOM cavity. Points represent experimental data and the continuous line represents the fit based on a rearrangement of (18).

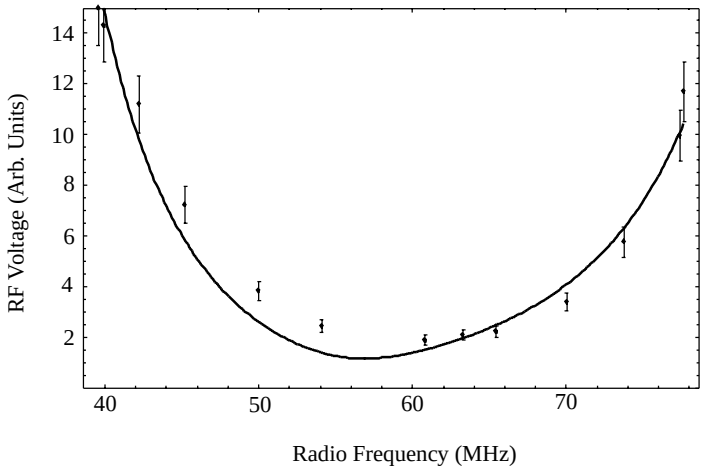

position of the AOM [9]. However, the signal intensity is expected to be reduced by a factor of ten compared to the Bragg regime. We note the signal intensity is above the minimum signal that can be detected with the heterodyne technique. Other challenges involved in building AOMs operating in the Raman–Nath regime include choosing a suitable AOM crystal to achieve a shorter transit time for the acoustic wave through the laser beam and using transducers with physical dimensions comparable to the expected beam waist ($\sim$10 μm).

7. Conclusions

The AOM-based retro-reflector discussed in this paper uses a readily available and relatively inexpensive device that is well understood. An important distinction in comparison to retro-reflectors discussed in refs. 2 and 3 is that this device offers the advantage of heterodyne detection. It also consists of a compact optical setup and requires an RF power of $\sim$2 W. We estimate the weight of the package to be $\sim$1 kg. Using nested optical components, we estimate the volume of the package to be $\sim$3000 cm^3. The maximum data transmission rate that can be achieved is higher than those given in refs. 2 and 3 but the field of view is reduced. Experiments were carried out in the Bragg regime and the results show that the field of view of the device is limited by the divergence angle of the laser beam and the acoustic beam. We investigated the effect of varying the radio frequency and drive power to determine the tuning range of the AOM cavity. This makes it possible to correct for effects of misalignment. Our results suggest that it is necessary to build the AOM on a rotation mount with servo control to realize the maximum field of view. Our estimates suggest that it should be possible to achieve a communication rate of $\sim$1 GHz in the Raman–Nath regime. Since it is possible for the laser to identify itself to the remote module, the device is suitable for secure, free-space optical communication. It is also possible to introduce a collection telescope with a large aperture and fiber couple its output into the device. The field of view of the device will then be limited by the field of view of the fiber ($\sim$15°). This will minimize the need to actively align the device. This will also make it possible to consider using this device for long-range communication links. However, the increase in the diameter of the laser beam at the output of the telescope will result in additional optical losses due to fiber coupling. Effects of laser beam propagation through the atmosphere can result in beam distortion and attenuation. To set up a communication link with a remote platform, it is necessary to implement a suitable tracking system. Although we do not address these issues, we note that they are common to all free-space communication devices [2, 3].

Acknowledgments

This research was supported by the Canada Foundation for Innovation, Ontario Innovation Trust, York University, and the Natural Sciences and Engineering Research Council of Canada.

References

1. J. Hecht. Laser Focus World, **11**, 101 (2001).
2. C.M. Swenson, C.A. Steed, I.A. De La Rue, and R.Q. Fugate. Proc. SPIE 2990. 1997. p. 298.
3. G.C. Gilbreath, W.S. Rabinovich, T.J. Meehan et al. Opt. Eng. **40**, 1348 (2001).
4. T. Mikaelian, M. Weel, A. Kumarakrishnan, P.R. Battle, and R.C. Swanson. Can. J. Phys. **81**, 639 (2003).
5. G. Spirou, T. Mikaelian, M. Weel, A. Vorozcovs, A. Andreyuk, A. Kumarakrishnan, P.R. Battle, and R.C. Swanson. CUPC, Quebec City. 2000.
6. G. Spirou, T. Mikaelian, M. Weel, A. Vorozcovs, A. Andreyuk, A. Kumarakrishnan, P.R. Battle, and R.C. Swanson. Bull. Am. Phys. Soc. **46**, 108 (2001).
7. G. Spirou, I. Yavin, M. Weel, T. Mikaelian, A. Vorozcovs, A. Andreyuk, A. Kumarakrishnan, P.R. Battle, and R.C. Swanson. Proceedings of the 23rd IEEE Aerospace Conference, Big Sky, Mont. 9–16 March 2002. IEEE Piscataway, N.J. Vol. 3, 1481 (2002).
8. R.R. Hayes. App. Opt. **40**, 6445 (2001).
9. B.E.A. Saleah and M.C. Teich. Fundamentals of photonics. John Wiley & Sons, Inc. 1991. Chapt. 20.
10. F.B.J. Buchkremer, R. Dumke, Ch. Buggle, G. Birkl, and W. Ertmer. Rev. Sci. Instrum. **71**, 3306 (2000).
11. R. Adler. IEEE Spectrum. May 1967. p. 42.
12. C.C. Davis. Lasers and electro-optics. Cambridge. 1996. Chapt. 19.
13. N. Uchida and N. Niizeki. Proc. IEEE **61**, 1073 (1973).
14. E.I. Gordon. Proc. IEEE **54**, 1391 (1966).
15. A. Siegman, M.W. Sasnett, and T.F. Johnston, Jr. IEEE J. Quantum Electron. **27**, 1098 (1991).